Geometry-based modelling of self-interference channels for outdoor scenarios

Sathya N. Venkatasubramanian, Chunqing Zhang, Leo Laughlin, Katsuyuki Haneda and Mark A. Beach

***Abstract*—In-band full-duplex (IBFD) transmission has the potential to nearly double the throughput by improving the spectral efficiency. To achieve this, the self-interference (SI) at the receiver due to one's own transmission must be suppressed, such that it does not obscure the desired signal. Compact on-frequency repeaters are suitable candidates for initial implementation of IBFD. However, the design, evaluation and optimisation of such systems requires realistic SI channel models. In this contribution, we characterize measured multiple-input multiple-output (MIMO) SI channels as a two-dimensional site-specific geometry-based stochastic channel model (GSCM). The model includes smooth walls causing specular reflections, diffuse scatterers along the smooth walls, and mobile scatterers modelling pedestrians and vehicles. Importantly, the model provides delay, angular and polarimetric characteristics of the MIMO SI channels, and is validated by comparing the measured and simulated channels in delay, Doppler and spatial domains.**

***Index Terms*—antenna, decoupling, isolation, MIMO, full-duplex.**

I. Introduction

IN-BAND FULL-DUPLEX (IBFD) transceivers [1]–[12] simultaneously transmit and receive radio frequency (RF) signals in the same frequency band. This has the potential to provide as much as double the capacity compared to traditional half-duplex systems, and reduce latency in wireless networks [6]. Transmitting and receiving on the same time-frequency resource results in strong co-channel *self-interference* (SI), which can be over 100 dB more powerful than the desired receive signal. Time and frequency division duplexing are established methods of *avoiding* co-channel SI. However, to achieve IBFD operation, the SI must be mitigated using various techniques to reduce and/or cancel SI at the receiver.

Relays and point-to-point radio links are among the first systems to deploy IBFD technologies [9], [13], [14], with commercial field trials now completed [15], [16]. One application for IBFD relays is outdoor-to-indoor coverage extension, where, the relay is deployed close to a window. In the downlink scenario, the relay decodes and/or amplifies signals from the base station towards users inside the building. In this type of system, SI results from direct coupling between the closely spaced transmit (Tx) and receive (Rx) antennas, and from indirect coupling due to multipath propagation between them, i.e., reflections and scattering in the operating environment. Previous results have demonstrated that this multipath propagation can result in significant SI [6], [8].

SI mitigation techniques can, in general, be divided into three categories: Over-the-air (OTA) SI avoidance [1], [5], [8], [13], RF SI cancellation [4], [8], [17], and digital baseband SI cancellation [4]. In case of OTA SI avoidance, separate antennas are used for Tx and Rx subsystems, thereby providing passive isolation by limiting electromagnetic coupling between the antennas. The effectiveness of OTA SI avoidance depends on design of the antenna position, pattern, and shielding and/or field absorption techniques [8]. This is then complemented further by RF and digital baseband SI cancellation techniques. RF SI cancellation techniques aim to suppress the SI in the analog receive-chain circuitry [6]. Passive feed-forward RF cancellation involves tapping the signal at the Tx antenna feed, processing this in the RF domain, and then subtracting this at the receiver [4]. Active feed-forward RF cancellation taps the signal in the digital baseband domain, and processes this to generate a baseband cancellation signal. This is then up-converted using an auxiliary transmitter and subtracted in the RF domain [18], [19]. Digital baseband SI cancellation is based on linear and non-linear SI channel estimation and subtraction in the digital baseband domain, see [6] and references therein.

Practical realization of IBFD radios requires mitigating the SI to the noise floor. This means that in addition to improving the electromagnetic isolation between the antennas, the multipath SI must be suppressed. The SI is also dynamic as objects in the environment are mobile, e.g., vehicles, pedestrians, etc. This necessitates knowledge of the SI channel behaviour to effectively mitigate the SI dynamically. Hence, the RF and baseband SI cancellation techniques need appropriate knowledge of the SI channel, and must be both wideband and adaptive over time [11], [20]. Thus, SI channel models play a vital role in the evaluation of the cancellation solutions. This paper focuses on the OTA SI avoidance, specifically, the measurement and modelling of the SI channel of an IBFD relay antenna system suitable for multiple-input-multiple-output (MIMO) systems.

Manuscript received 02 April 2017. Revised manuscript accepted 09 December 2018.

Sathya N. Venkatasubramanian and Katsuyuki Haneda are with the Department of Electronics and nanoengineering, Aalto University, School of Electrical Engineering, Espoo, Finland

Chunqing Zhang, Leo Laughlin, and Mark A. Beach are with the Department of Electrical and Electronic Engineering, University of Bristol, Bristol, United Kingdom.

The research work leading to these results was funded by the Academy of Finland, under the project "In-band Full-Duplex MIMO Transmission: A Breakthrough to High-Speed Low-Latency Mobile Networks", the Finnish Funding Agency for Technology and Innovation, Tekes, under the project "Full-Duplex Cognitive Radio: Technology and Application to Cognitive M2M Communications", the Aalto ELEC doctoral school, Finland, the UK Engineering and Physical Sciences Research Council, under the project "Scalable Full-Duplex Dense Networks (SENSE)", and the University of Bristol, UK.

Color versions of one or more of the figures in this paper are available online at http://ieeexplore.ieee.org.

Digital Object Identifier:

The SI channel includes dynamic multipath coupling due to movement of objects in the physical environment.

Previous work on SI channel characterisation for an IBFD relay [21] investigated the mean isolation level at 2.6 GHz for indoor deployment, and did not discuss the wideband characteristics of the SI channel. The paper [22] reports indoor wideband SI channels between 2.45 to 2.75 GHz based on measurements, but still lacks the spatial and Doppler characteristics. This paper presents the first channel model based on measurements, which jointly models the SI channel in the polarization, delay, Doppler and spatial domains. Understanding SI propagation in all of these domains is critical in the development and evaluation of IBFD radios. This paper extends the work [22], with the following three major advances.

1) Performing additional measurements to cover various deployment scenarios of IBFD relays,
2) Characterising the SI channels in terms of delay, Doppler, spatial and polarisation domains in addition to the already-reported wideband characteristics, and finally,
3) Establishing a site-specific geometry-based stochastic channel model (GSCM), in a similar spirit as [23], [24], which can be used as a versatile tool to reproduce the SI channel over spatial, temporal, delay and polarisation domains jointly.

The Tx and Rx antennas are located close to each other in the proposed GSCM, compared to the site-specific GSCM developed for vehicular-to-vehicular scenario in [23]. Furthermore, the proposed GSCM includes polarization dependency which is not considered in [23].

The remainder of this paper is organised as follows. Section II describes the measurement setup, modes and scenario. Section III describes the measured SI channel characteristics, which are then modelled as a site-specific GSCM as described in Section IV. Section V describes the channel model validation and Section VI concludes the paper.

II. SI Channel Measurements

A. Antenna Array

For the wideband and time-varying MIMO SI channel measurements, a compact relay antenna system consisting of back-to-back patch antennas was chosen. It has dimensions of $180 \times 150 \times 57\text{mm}^3$ as previously reported in [22]. The relay comprises two ground planes spaced 47 mm apart using nylon screws. Two dual-polarised patch antennas are located on either side of the ground planes facing opposite directions, corresponding to four feeds on each side. We assume that the four feed ports on one side serve as Tx antennas, and another four on the other side serve as Rx antennas. In total, we have $4 \times 4 = 16$ coupling channels between the Tx and Rx feeds. Of these, eight are between Tx and Rx antenna feeds with the same polarisation, and the other eight are between antenna feeds with orthogonal polarisations.

The individual antenna feeds have input matching better than -6 dB over around 300 MHz bandwidth across 2.6 GHz.

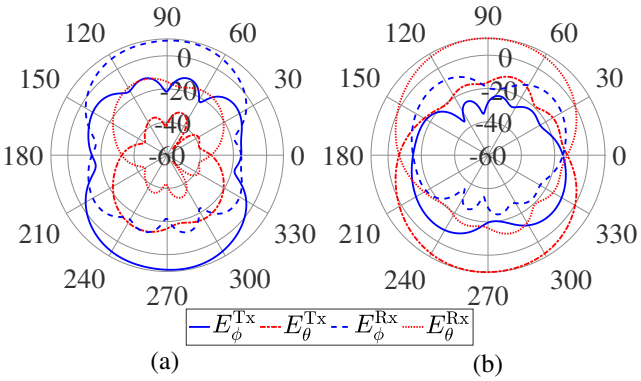

Fig. 1. Simulated radiation patterns of a single Tx-Rx antenna pair in the azimuth plane for (a) horizontally polarised antennas, and (b) vertical polarised antennas.

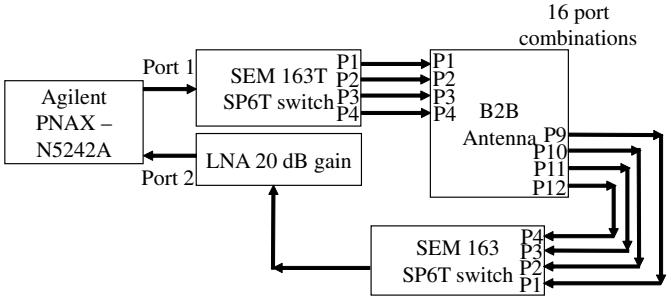

Fig. 2. Schematic of the SI measurement setup with the 4×4 MIMO back-to-back (B2B) antenna connected to the VNA using SP6T switches.

The mutual coupling between the antenna feeds in the anechoic chamber, which refers to the direct coupling in the SI channel, varies between -40 to -80 dB for different antenna combinations. Fig. 1 shows the simulated azimuth radiation patterns of the horizontally (H) and vertically (V) polarised Tx and Rx antennas with respect to the ground. The antennas have a main lobe gain of 9.3 dBi in the respective broadside directions. Due to the back-to-back structure of the relay, their broadsides point in opposite directions.

B. SI Channel Measurements

The dynamic wideband MIMO SI channel measurements were performed using an Agilent PNAX-N5242 Vector Network Analyzer (VNA). The VNA performs continuous-wave measurements of channels between 2.45 and 2.75 GHz with 0.5 MHz spacing. The measurement setup is illustrated in Fig. 2. Port 1 of the VNA was used as a transmitting port and connected to antenna feeds 1-4 through a SP6T switch (Narda SEM163T). The two unused ports of the RF switch were terminated by 50 Ω loads. Feeds 9-12 were connected to another SP6T switch (Narda SEM163) in a similar configuration, and was then connected to a low noise amplifier (LNA) with 20 dB gain before it is fed to Port 2 of the VNA. The scattering parameters, S_{21} of the SI channel were measured for different antenna combinations over time. The switches were mounted at the base of the antenna tripod, and were controlled using a custom microcontroller and logic circuit

with a serial RS-232 interface. The switches and VNA were interfaced using MATLAB codes. The effect of the internal circuits of the VNA, cables, switches and LNA were removed in post-processing using the back-to-back calibration method.

C. Measurement Modes

In this section, we describe the different modes of the measurement setup to model the delay and Doppler characteristics.

1) Static mode: The multipath SI channel measurements were performed at multiple positions, i.e., different antenna locations and heights. The S_{21} was measured sequentially for different feed combinations using the RF switches to obtain the 4×4 MIMO SI channels. A complete measurement of the MIMO channel takes 640 ms including the switching delay. At each antenna position, the MIMO channel was measured 10 times.

2) Doppler mode: In order to characterise the temporal fading characteristics of the SI channel, the S_{21} is repeatedly measured at higher temporal sampling rates than the static mode. Because of the relatively slow RF mechanical switches, these measurements were conducted only for one antenna feed combination at a time. Moreover, due to the limited memory available on board the VNA, there is a trade-off between the temporal sampling rate and the duration of the measurement. The VNA was configured to use a *segmented sweep* mode, in which multiple sweeps are stored into the same trace buffer, avoiding accessing the memory during the sweeps. In this mode, the sampling rate is limited only by the sweep time and the local oscillator fly-back time. For the 300 MHz bandwidth and 0.5 MHz frequency resolution, this configuration allows us to measure channels every 7 ms. This leads to a Doppler bandwidth of 142 Hz, which corresponds to 71 Hz maximum Doppler shift. However, due to the limited trace buffer size, the number of sweeps was also limited to 20 per measurement, with each sweep repeatedly sampling across the entire bandwidth 50 times. This results in a sampling duration of $7\text{ms} \times 50 = 350\,\text{ms}$, corresponding to 2.86 Hz resolution of the Doppler spectra. Due to the large measurement time taken for the Doppler characterisation, only two feed combinations, one *co-* polarised and one *cross-* polarised were measured.

D. Measurement Scenario

The SI channels were measured outside a building window at the street level on Park Row, Bristol, adjacent to the Merchant Venturers Building at the University of Bristol. This street has three story buildings on both sides of the road, forming a street canyon. Measurements were taken at three locations adjacent to the window, repeated at 11 antenna heights between 170 cm and 190 cm with 2 cm increment, resulting in 33 measurement positions in this measurement scenario. The antenna was oriented with the main beams facing out of the window/into the room. The antenna was located 30 cm in front of the windows.

III. SI Channel Characteristics

In this section, the delay, temporal and spatial domain characteristics of the measured SI channels are discussed by means of the power delay profile (PDP), power Doppler spectra (PDS) and antenna correlation.

A. Delay Domain Characteristics

1) Derivation of PDPs: The static mode measurements described in Section II-C are used for deriving the PDPs. The wideband time-varying MIMO SI channels are described by the transfer function $H_{ij}(f,t,p)$, where i and j are the Rx and Tx antenna indices, respectively; f denotes the measurement radio frequency index, t refers to the measurement time index at the antenna position, $1 \leq t \leq 10$, corresponding to 10 realizations of $\boldsymbol{H}(f,t,p)$ obtained over time as described in Section II-C; p refers to the antenna position index, $1 \leq p \leq 33$ as described in Section II-D.

The channel impulse response (CIR) of each antenna combination $h_{ij}(m,t,p)$ is obtained by the Inverse Fast Fourier transform (IFFT) of $H_{ij}(f,t,p)$ with the Hann window; m refers to the delay bin index defined every 3.33 ns corresponding to 300 MHz measurement bandwidth. The Hann window was chosen as it has low levels of signal leakage in the delay domain, allowing weaker parts of the SI channel to be detected properly. The amplitude of each impulse response is then scaled with a factor of 0.5 to account for the reduction of the main-lobe power due to the Hann window.

The PDP for each feed combination is obtained from the CIRs as

$$PDP_{ij}(m) = E_{t,p}\{|h_{ij}(m,t,p)|^2\}, \tag{1}$$

thereby removing the effect of small scale fading; $E_{t,p}\{\cdot\}$ refers to the ensemble average with respect to realizations over time t and position p. A single PDP for each antenna feed combination is therefore defined for the measurement *scenario*.

The *polarisation-specific* PDPs i.e., *co-* polarised feed combinations, V-V, H-H, and *cross-* polarised feed combinations, V-H and H-V, are calculated as the ensemble average of the PDPs between the respective feed combinations. The polarizations V and H are with respect to the ground. Here, the polarization-pair corresponds to the Rx-Tx antenna polarizations. The *global* PDP is derived as the ensemble average of the PDPs over all the feed combinations.

A peak in the PDP is identified at a particular delay bin if the power in the delay bin is 3 dB larger than the 7-bin moving average of the PDP, centred at the delay bin. In addition, the first three delay bins, i.e., 0 ns, 3.33 ns and 6.67 ns are identified as peaks. When the peak delay bins are detected, accurate peak delays and powers are determined by fitting the local PDP shape around the peak delay bin with a Sinc function for interpolation. The Sinc function in the delay domain corresponds to a rectangular frequency window of the transfer function. For the interpolation, the PDP is calculated from the CIRs that are obtained from the transfer function using a rectangular window instead of the Hann window.

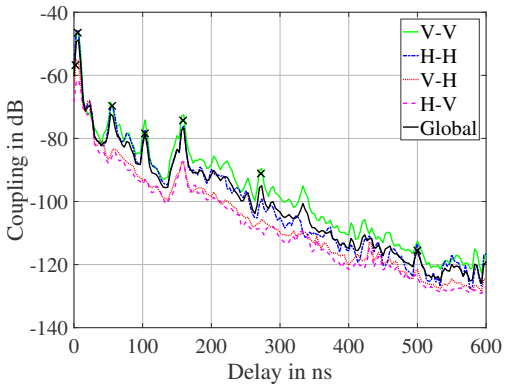

Fig. 3. Measured PDPs indicating *polarisation-specific* PDPs obtained from the ensemble average of the PDPs with the corresponding antenna polarisations, and the *global* PDP with specular peaks.

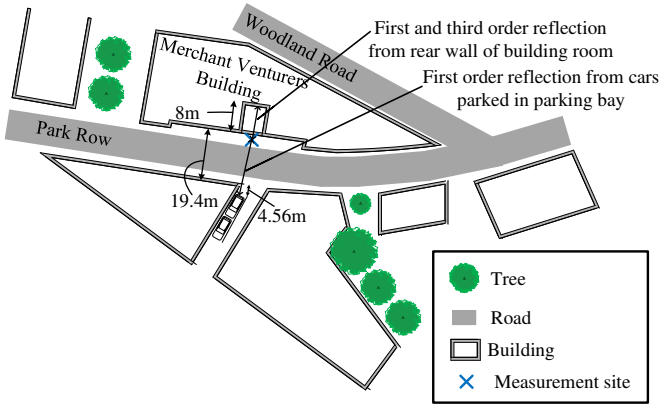

Fig. 4. Schematic of measurement site with antenna deployed outside building window.

2) Scatterer identification: Fig. 3 shows the measured *global* and *polarisation-specific* PDPs. The objects causing the specular peaks are identified based on the geometry of the measured scenario and matching them to the corresponding delays of the peaks. The main objects causing the specular reflections are indicated in Fig. 4. This includes the walls of the room inside the building adjacent to the antenna deployment location, as well as the buildings and small scatterers on the other side of the road. The measured PDP in Fig. 3 shows that the V-V polarized component is stronger than the H-H polarized component. This is because, the measured SI channel is affected by antenna radiation patterns. The vertically polarized antennas used in the measurements have larger beamwidth compared to the horizontally polarized antennas as shown in the simulated radiation patterns in Fig. 1. This results in stronger measured SI for the V-V polarizations as compared to the H-H polarizations, while V-H and H-V polarized feed combinations have similar levels of PDPs.

3) Delay dispersion: The delay dispersion of the SI channel is represented by the mean delay, τ_{m} and the RMS delay spread, τ_{rms}. They are calculated from the *global* and *polarisation-specific* PDPs in the manner defined in [25]. Since the SI cancellation aims to suppress the SI to the noise floor, all delay bins with power above the noise threshold are used in their calculation. The noise threshold is given by $P_{\mathrm{th}} = P_{\mathrm{n}} + 6$ dB where P_{th} and P_{n} are noise threshold and estimated noise from the PDPs, respectively. The *global* RMS delay spread is 10.7 ns with mean delay of 6.5 ns indicating that most of the SI power arrives within the first four delay bins.

4) Wideband fading characteristics: The wideband fading characteristics of the SI channel are modelled by estimating the Ricean K-factor of each delay bin through the moment-based method [26]. The fading realizations come from the CIRs of the MIMO channel at different antenna positions. The magnitudes of the CIRs are normalized to that of the PDP of the corresponding antenna combination as

$$a_{ij}(m,t,p) = |h_{ij}(m,t,p)|^2 / PDP_{ij}(m). \tag{2}$$

The Ricean K-factors for the first two delay bins at 0 ns and 3.33 ns are 5.1 dB and 0.3 dB respectively. This is due to the direct component. The remaining delay bins exhibit Rayleigh fading, i.e., $K \leq 0$ dB due to several multipaths arriving at the same delay bin.

B. Doppler characteristics

Moving objects, such as pedestrians and cars in the surrounding environment, cause SI channel variation in the time-domain. The Doppler measurement mode described in Section II-C is therefore our main interest in this subsection. The transfer functions for the measured *co-* and *cross-* polarised feed combinations, $H_{\mathrm{co}}(f,t,p,n)$ and $H_{\mathrm{cross}}(f,t,p,n)$ respectively, are defined in the same manner as Section III-A; $n = 1, 2, ..., 20$ refers to the measurement sweep index at the same antenna position as described in Section II-C.

The corresponding CIRs, $h_{\mathrm{co}}(m,t,p,n)$ and $h_{\mathrm{cross}}(m,t,p,n)$ are obtained using the IFFT in a similar manner as described in Section III-A. The spreading functions [25], $S_{\mathrm{co}}(m,\nu,p,n)$ and $S_{\mathrm{cross}}(m,\nu,p,n)$ are derived by applying the FFT to the series of CIRs over time index, $1 \leq t \leq 50$, sampled every 7 ms at each position. This leads to the delay-Doppler representation of the channel with Doppler frequency ν. The PDS for the *co-* and *cross-*polarised channels are obtained by incoherently averaging the spreading functions as

$$\begin{aligned} PDS_{\mathrm{co}}(m,\nu,p) &= E_n\{|S_{\mathrm{co}}(m,\nu,p,n)|^2\}, \\ PDS_{\mathrm{cross}}(m,\nu,p) &= E_n\{|S_{\mathrm{cross}}(m,\nu,p,n)|^2\}, \end{aligned} \tag{3}$$

where $E_n\{\cdot\}$ denotes the ensemble average over the measurement sweeps at the same antenna position. The mean Doppler shift, ν_{m} and the RMS Doppler spread, ν_{rms} are calculated at each delay bin and antenna position as defined in [25], considering only Doppler bins with power greater than the noise floor of the measurements. The means of ν_{m} and ν_{rms} across antenna positions, $\overline{\nu_{\mathrm{m}}}(m)$ and $\overline{\nu_{\mathrm{rms}}}(m)$ respectively, are then calculated at each delay bin for the *co-* and *cross-* polarisations. The *global* mean Doppler shift and RMS Doppler spread are finally given by the mean of $\overline{\nu_{\mathrm{m}}}(m)$ and $\overline{\nu_{\mathrm{rms}}}(m)$ over the *co-* and *cross-* polarised feed combinations. Fig. 5 shows the *global* mean Doppler shift and RMS Doppler spread, as well as the *co-* and *cross-* polarised

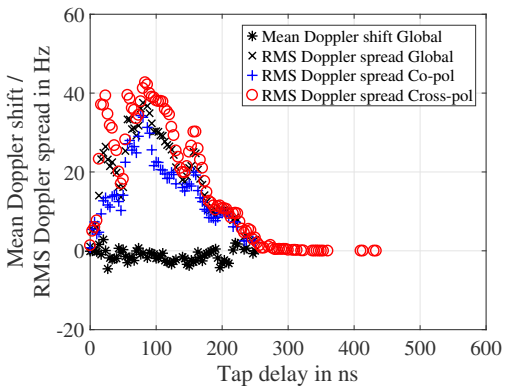

Fig. 5. Measured mean Doppler shift and RMS Doppler spreads.

RMS Doppler spreads. Based on the location of vehicle and pedestrian traffic, the Doppler spread up to 40 ns delay is primarily due to pedestrian movement, while beyond 40 ns delay, the Doppler spread is attributed to both pedestrian and vehicular movement. The RMS Doppler spread for the *co-* and *cross-* polarisations follow a similar pattern. Also, a wooden door was ~ 2 m away from the antenna site, which was opened and closed frequently, with people walking towards and away from the antenna. This can cause additional Doppler spread in the initial delay bins.

C. Spatial characteristics

We finally derive the narrowband antenna correlation of the SI MIMO channel as a measure of spatial and polarimetric characteristics. The static mode measurements are used for the analysis.

The narrowband antenna correlation between the j-th and k-th Tx antenna ρ_{jk}^{Tx} is defined as

$$\rho_{jk}^{\mathrm{Tx}}(t,p) = \frac{\sum_{i=1}^{4}\left(|H_{ij}| - \overline{|H_j|}\right)\left(|H_{ik}| - \overline{|H_k|}\right)}{\sqrt{\sum_{i=1}^{4}\left(|H_{ij}| - \overline{|H_j|}\right)^2}\cdot\sqrt{\sum_{i=1}^{4}\left(|H_{ik}| - \overline{|H_k|}\right)^2}}, \tag{4}$$

where i refers to the Rx antenna index, $\overline{|H_j|} = E_{f,i}\{|H_{ij}|\}$. For convenience, the time index, t, frequency index, f, and position index, p, dependence is suppressed in the right hand side of (4). The mean antenna correlation over time and position is calculated as

$$\overline{\rho}_{jk}^{\mathrm{Tx}} = E_{t,p}\{\rho_{jk}^{\mathrm{Tx}}(t,p)\}. \tag{5}$$

The narrowband correlation between the Rx antenna elements is calculated in a similar manner. The antenna correlation is found less than 0.6, indicating large angular dispersiveness of the channel. This may lead to limited performance of eigenmode-based SI mitigation techniques [27].

IV. SI Channel Model

A site-specific GSCM is developed based on the SI channel characteristics described in Section III for the outdoor deployment of IBFD relays. First, the site-specific geometry is defined, and then a method to reproduce the SI channel as a sum of propagation paths is given. Finally, the implementation recipe is enumerated to generate dynamic wideband MIMO SI channel.

A. Geometry description

The schematic of the proposed two-dimensional geometry is illustrated in Fig. 6. It comprises smooth building walls on both sides of the road, as well as the smooth walls of the room inside the building next to the antenna deployment location. In addition, we model diffuse scatterers placed adjacent to the smooth walls, and mobile scatterers, i.e., pedestrians and vehicles on the road.

The length and width of the road is defined along the x- and y-axes, respectively. The coordinate limits of the geometry along the y dimension is determined by the road width W_{road} and the room depth D_{room} next to the antenna, as shown in Fig. 6. The origin is located at the centre of the road. The coordinate limits along the x dimension is determined by the maximum delay $\tau_{\max}$ due to first order diffuse scattering from objects on both sides of the antenna, along the x axis. Since the Tx and Rx antennas are co-located, $x_{\min} = x_{\mathrm{Tx}} - \tau_{\max}c/2$ and $x_{\max} = x_{\mathrm{Tx}} + \tau_{\max}c/2$ where x_{Tx} corresponds to the x-coordinate of the Tx and c is the velocity of light. The characteristics of reflected and scattered paths due to different walls and scatterers are defined as follows.

1) Smooth walls: The building walls on both sides of the road are at $y = \pm W_{\mathrm{road}}/2$ and extend from $x_{\min}$ to $x_{\max}$. The walls of the room behind the antenna are also defined as smooth walls with dimensions $W_{\mathrm{room}} \times D_{\mathrm{room}}$. Each wall is assigned corresponding permittivities and normal vectors. Up to N_{w}-th order reflections from the walls are considered. The complex signal amplitude of the l-th reflected path $\boldsymbol{\alpha}_{\mathrm{wall}}^{l}$ is

$$\boldsymbol{\alpha}_{\mathrm{wall}}^{l} = \left(\frac{\lambda}{4\pi d_l}\right)^{n_{\mathrm{l}}/2} e^{j\xi_l} \prod_{n_{\mathrm{w}}=1}^{N_{\mathrm{w}}} \begin{bmatrix} \Gamma_{\mathrm{VV}}^{(n_{\mathrm{w}})} & 0 \\ 0 & \Gamma_{\mathrm{HH}}^{(n_{\mathrm{w}})} \end{bmatrix}, \tag{6}$$

where λ is the free space wavelength and d_l is the propagation path length; $\Gamma_{\mathrm{VV}}^{(n_{\mathrm{w}})}$ and $\Gamma_{\mathrm{HH}}^{(n_{\mathrm{w}})}$ are the Fresnel reflection coefficients at the n_{w}-th interaction of the path with the smooth wall for the respective polarisations in (6). A random phase $\xi_l \sim U[0, 2\pi]$ is added to each path to account for the phase change due to ground reflections of the corresponding paths. The path loss exponent, n_{l} is defined as

$$n_{\mathrm{l}} = \begin{cases} 2.2 & \text{if } d_l \le d_{\mathrm{break}} \\ 3.3 & \text{if } d_l > d_{\mathrm{break}} \end{cases}, \tag{7}$$

where $d_{\mathrm{break}} = 4{h_{\mathrm{ant}}}^2/\lambda$ is the breakpoint distance where the ground begins obstructing the first Fresnel zone; h_{ant} refers to the Tx/Rx antenna height. The higher path loss exponent $n_{\mathrm{l}} > 2$ is a reasonable estimate considering the low antenna height, obstruction of paths' first Fresnel zone due to the ground, as well as reflections from the ground [28].

If the signal penetrates through the glass window near the antenna, the corresponding path undergoes additional penetration loss, determined by the polarimetric transmission coefficients. In addition, 10 dB losses are added to paths if

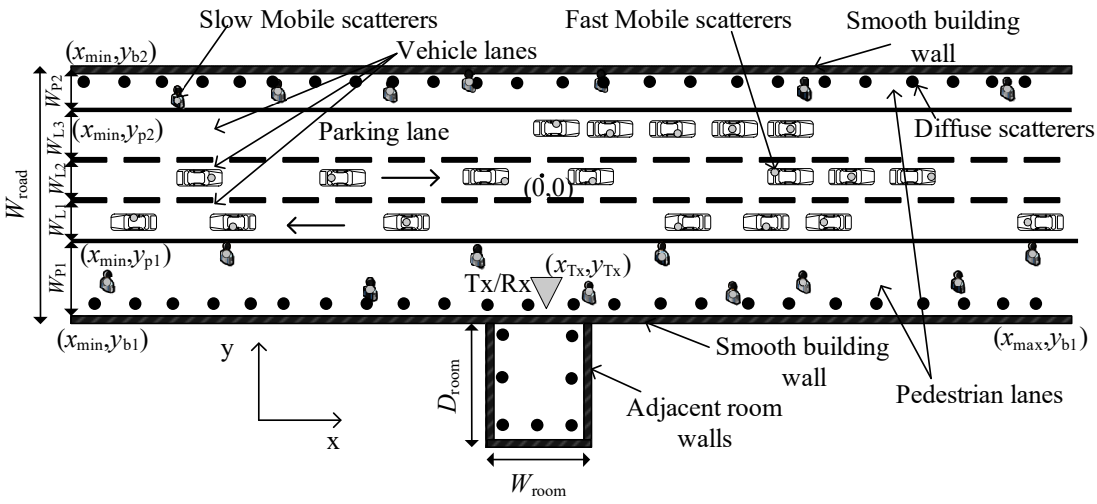

Fig. 6. Schematic of the proposed site-specific geometry for the dynamic wideband MIMO SI channel model. The x- and y-coordinates, and scatterer density are representative and not to scale. $W_{\mathrm{P}i}$ and $W_{\mathrm{L}i}$ denotes width of the i-th pedestrian and vehicle lanes including parking lanes respectively.

they are shadowed by the relay antenna itself; such paths occur when thinking of twice-reflection on both sides of the walls for example. The 10 dB additional loss is a reasonable estimate when considering the shadowed Fresnel zone size at 2.6 GHz. The angle-of-arrival (AoA) ϕ^l_{AoA}, and angle-of-departure (AoD) ϕ^l_{AoD} of the l-th reflected path is calculated at the co-located Tx/Rx antenna location.

2) Diffuse scatterers adjacent to smooth walls: Next, we consider diffuse scatterers located next to smooth walls, which correspond to objects such as sign boards and rough brick walls. These diffuse scatterers are located at a small distance, i.e. 5 cm in front of the smooth walls and are uniformly spaced along them with density $\lambda_{\mathrm{diffuse}}$. Each diffuse scatterer is assigned a Radar Cross Section (RCS) with isotropic scattering. Due to the cluttered street canyon environment as well as the operating radio frequency of 2.6 GHz, both first order and second order diffuse scattering are considered. The polarimetric complex amplitude of a path arising from the s-th diffuse scatterer is given by

$$\boldsymbol{\alpha}^s_{\mathrm{diffuse}} = \frac{\lambda}{4\pi {d_s}^2}\sqrt{\frac{\sigma_s}{4\pi}}\cdot\boldsymbol{\gamma}_s, \tag{8}$$

where d_s corresponds to the distance of the scatterer from the co-located Tx/Rx antenna location and $\sigma_s = \sigma_{\mathrm{diffuse}}$ is the RCS of the corresponding scatterer in (8). The distance term is squared indicating equal path length from the Tx antenna to the scatterer and from the scatterer back to the Rx antenna. Thus, the total path distance is $d_{s1} = 2d_s$. $\boldsymbol{\gamma}_s$ denotes the polarisation matrix, defined as

$$\boldsymbol{\gamma}_s = \begin{bmatrix} e^{j\xi^s_{11}} & \frac{e^{j\xi^s_{12}}}{\sqrt{CPR\cdot XPD_{\mathrm{H}}}} \\ \frac{e^{j\xi^s_{21}}}{\sqrt{XPD_{\mathrm{V}}}} & \frac{e^{j\xi^s_{22}}}{\sqrt{CPR}} \end{bmatrix}, \tag{9}$$

where CPR, XPD_{V} and XPD_{H} in (9) refer to the *co-* and *cross-* polar power ratios between the vertical and horizontal polarizations as given by

$$CPR = \frac{P_{\mathrm{VV}}}{P_{\mathrm{HH}}},\quad XPD_{\mathrm{V}} = \frac{P_{\mathrm{VV}}}{P_{\mathrm{HV}}},\quad XPD_{\mathrm{H}} = \frac{P_{\mathrm{HH}}}{P_{\mathrm{VH}}}. \tag{10}$$

The phase of each element of the polarization matrix is assigned randomly for each of the scattered paths, $\xi^s_{ij} \sim U[0, 2\pi]$.

The complex polarimetric amplitude of the second order scattered paths from the diffuse scatterers s_1 and s_2 is given by

$$\boldsymbol{\alpha}^{s_1 s_2}_{\mathrm{diffuse}} = \frac{\lambda}{4\pi d_{s_1} d_{s_2} d_{s_1 s_2}}\frac{\sqrt{\sigma_{s_1}\sigma_{s_2}}}{4\pi}\cdot\boldsymbol{\gamma}_{s_1 s_2}, \tag{11}$$

where d_{s_1} and d_{s_2} correspond to the distance between the co-located Tx/Rx antennas and the scatterers s_1 and s_2 respectively, and $d_{s_1 s_2}$ refers to the distance between the two scatterers in (11). The total path length is thus, $d_{s_1,s_2} = d_{s_1} + d_{s_2} + d_{s_1 s_2}$. σ_{s_1} and σ_{s_2} refer to the RCS of the corresponding scatterers. $\boldsymbol{\gamma}_{s_1 s_2}$ is defined in a similar manner as (9).

It should be noted that the diffuse paths from the room adjacent to the antenna will have additional penetration loss as the signal penetrates through the glass windows, similar to the paths from smooth walls. Also, we assume that the diffuse scatterers inside the room do not interact with the diffuse scatterers outside the room on the road, and thus, $\boldsymbol{\alpha}^{s_1 s_2}_{\mathrm{diffuse}} = 0$ in that case. No diffuse scatterers are considered with $d_{s1}, d_{s_1 s_2} < 2\,\mathrm{m}$ as these scatterers are observed to be in the near-field region of the antennas.

3) Mobile scatterers: Finally, the pedestrians and vehicles are modelled as mobile scatterers in their respective lanes with corresponding velocities. The two pedestrian lanes are located adjacent to the building walls. The initial positions of pedestrian mobile scatterers in the x-dimension are uniformly and randomly distributed, such that $x_{s_{\mathrm{slow}}}(t=0) \sim U[x_{\min}, x_{\max}]$, where s_{slow} refers to the pedestrian index. The pedestrian density λ_{slow} determines the number of pedestrians in the geometry. The corresponding y-coordinate of the pedestrian scatterers is similarly derived as $y_{s_{\mathrm{slow}}} \sim U[y_{\mathrm{b1}}, y_{\mathrm{p1}}]$. The x- and y- coordinates of pedestrians mobile scatterers on the other side of the road are also randomly generated based on a uniform distribution with the corresponding range $y_{s_{\mathrm{slow}}} \sim U[y_{\mathrm{p2}}, y_{\mathrm{b2}}]$; see Fig. 6 for the definitions of $y_{\mathrm{b1}}, y_{\mathrm{p1}}, y_{\mathrm{p2}}$, and

$y_{\mathrm{b}2}$. The velocity of each pedestrian scatterer along the x-axis is determined as $v_{s_{\mathrm{slow}}} \sim U[-v_{\max}^{\mathrm{slow}}, v_{\max}^{\mathrm{slow}}]$, with maximum speed $v_{\max}^{\mathrm{slow}}$. We consider that there is no pedestrian movement along the y-axis.

In a similar manner, the scatterers representing fast-moving vehicles are distributed randomly in the x-dimension as $x_{s_{\mathrm{fast}}}(t=0) \sim U[x_{\min}, x_{\max}]$ with density λ_{fast}, where s_{fast} is the vehicle index. The y coordinate is then determined as $y_{s_{\mathrm{fast}}} \sim U[y_{\mathrm{p}1}, y_{\mathrm{p}2}]$, where the coordinates $y_{\mathrm{p}1}, y_{\mathrm{p}2}$ are defined in Fig. 6. The vehicles in lanes L_1 and L_2 move along $-x$ and $+x$ directions respectively, while lane L_3 is designated as a parking lane. A direction parameter v_s is assigned to each vehicular scatterer, and can take either -1 or $+1$, representing the movement in $-x$ and $+x$ directions respectively. The speed of vehicles is determined by Poisson distribution as $v_{s_{\mathrm{fast}}} \sim \mathrm{Poisson}(v_{\mathrm{fast}})$, where v_{fast} corresponds to the mean speed in either direction; $v_{\mathrm{fast}} = 0$ for vehicles in the parking lane.

Each mobile scatterer is assigned an RCS, $\sigma_{\mathrm{mobile}} \in \{\sigma_{\mathrm{slow}}, \sigma_{\mathrm{fast}}\}$, corresponding to pedestrians and vehicles respectively, and is assumed to exhibit isotropic scattering. Only first order scattering is considered from the mobile scatterers. The polarimetric complex amplitude of a path arising from the s_{m}-th mobile scatterer, $s_{\mathrm{m}} \in \{s_{\mathrm{slow}}, s_{\mathrm{fast}}\}$, $\boldsymbol{\alpha}_{\mathrm{mobile}}^{s_{\mathrm{m}}}$ is calculated in a similar manner as the first order diffuse scattering in (8), such that

$$\boldsymbol{\alpha}_{\mathrm{mobile}}^{s_{\mathrm{m}}} = \frac{\lambda}{4\pi {d_{s_{\mathrm{m}}}}^2} \sqrt{\frac{\sigma_{\mathrm{mobile}}}{4\pi}} \cdot \boldsymbol{\gamma}_{s_{\mathrm{m}}}, \tag{12}$$

where $d_{s_{\mathrm{m}}}$ is the distance between the co-located Tx-Rx antennas and the mobile scatterer, resulting in total path distance $d_{s_{\mathrm{m}1}} = 2d_{s_{\mathrm{m}}}$, and where $\boldsymbol{\gamma}_{s_{\mathrm{m}}}$ is defined in a similar manner as (9).

B. Channel generation

Once the delay, amplitude, AoA and AoD are defined for the reflected and scattered paths, they are combined with the antenna radiation patterns to yield the radio channel transfer function H_{ij} as

$$\begin{aligned} H_{ij} =& H_{ij,\mathrm{direct}} + \sum_{l=1}^{L} H_{ij,\mathrm{wall}}^{l} + \sum_{s=1}^{L_{\mathrm{diffuse}}} H_{ij,\mathrm{diffuse}}^{s} \\ &+ \sum_{s_1=1}^{L_{\mathrm{diffuse}}} \sum_{s_2=1, s_2\neq s_1}^{L_{\mathrm{diffuse}}} H_{ij,\mathrm{diffuse}}^{s_1 s_2} + \sum_{s_{\mathrm{m}}=1}^{L_{\mathrm{mobile}}} H_{ij,\mathrm{mobile}}^{s_{\mathrm{m}}} \end{aligned}, \tag{13}$$

where L, L_{diffuse} and L_{mobile} correspond to the number of reflected paths from smooth walls, and the number of diffuse and mobile scatterers, respectively; $H_{ij,\mathrm{direct}}$ denotes the mutual coupling between the Tx and Rx antennas, which comes either from electromagnetic simulations or measurements of the considered IBFD relay. Each term in (13) is obtained by combining the radiation patterns of the Tx and Rx antennas with the corresponding polarimetric complex path response.

For smooth wall reflections, the transfer function of the l-th path, $H_{ij,\mathrm{wall}}^{l}$ is

$$H_{ij,\mathrm{wall}}^{l} = \begin{bmatrix} E_{\mathrm{V},i}^{\mathrm{Rx}}(\phi_{\mathrm{AoA}}^{l}) \\ E_{\mathrm{H},i}^{\mathrm{Rx}}(\phi_{\mathrm{AoA}}^{l}) \end{bmatrix}^{T} \boldsymbol{\alpha}_{\mathrm{wall}}^{l} \begin{bmatrix} E_{\mathrm{V},j}^{\mathrm{Tx}}(\phi_{\mathrm{AoD}}^{l}) \\ E_{\mathrm{H},j}^{\mathrm{Tx}}(\phi_{\mathrm{AoD}}^{l}) \end{bmatrix} \times e^{-j2\pi d_l f/c}, \tag{14}$$

where $E_{\mathrm{V},i}^{\mathrm{Rx}}(\phi_{\mathrm{AoA}}^{l})$, $E_{\mathrm{H},i}^{\mathrm{Rx}}(\phi_{\mathrm{AoA}}^{l})$, $E_{\mathrm{V},j}^{\mathrm{Tx}}(\phi_{\mathrm{AoD}}^{l})$ and $E_{\mathrm{H},j}^{\mathrm{Tx}}(\phi_{\mathrm{AoD}}^{l})$ correspond to the complex amplitude of the i-th receive and j-th transmit antenna in the azimuth plane for vertical and horizontal polarisations respectively; $\cdot^{T}$ is the transpose of the matrix, $\boldsymbol{\alpha}_{\mathrm{wall}}^{l}$ is given by (6). Similarly, the channel transfer functions for the first and second order diffuse paths $H_{ij,\mathrm{diffuse}}^{s}$ and $H_{ij,\mathrm{diffuse}}^{s_1 s_2}$, and mobile scatterers $H_{ij,\mathrm{mobile}}^{s_{\mathrm{m}}}$ in (13) are

$$\begin{aligned} H_{ij,\mathrm{diffuse}}^{s} = & \begin{bmatrix} E_{\mathrm{V},i}^{\mathrm{Rx}}(\phi_{\mathrm{AoA}}^{s}) \\ E_{\mathrm{H},i}^{\mathrm{Rx}}(\phi_{\mathrm{AoA}}^{s}) \end{bmatrix}^{T} \boldsymbol{\alpha}_{\mathrm{diffuse}}^{s} \begin{bmatrix} E_{\mathrm{V},j}^{\mathrm{Tx}}(\phi_{\mathrm{AoD}}^{s}) \\ E_{\mathrm{H},j}^{\mathrm{Tx}}(\phi_{\mathrm{AoD}}^{s}) \end{bmatrix} \\ & \times e^{-j2\pi d_{s1} f/c}, \end{aligned} \tag{15}$$

$$\begin{aligned} H_{ij,\mathrm{diffuse}}^{s_1 s_2} = & \begin{bmatrix} E_{\mathrm{V},i}^{\mathrm{Rx}}(\phi_{\mathrm{AoA}}^{s_1 s_2}) \\ E_{\mathrm{H},i}^{\mathrm{Rx}}(\phi_{\mathrm{AoA}}^{s_1 s_2}) \end{bmatrix}^{T} \boldsymbol{\alpha}_{\mathrm{diffuse}}^{s_1 s_2} \begin{bmatrix} E_{\mathrm{V},j}^{\mathrm{Tx}}(\phi_{\mathrm{AoD}}^{s_1 s_2}) \\ E_{\mathrm{H},j}^{\mathrm{Tx}}(\phi_{\mathrm{AoD}}^{s_1 s_2}) \end{bmatrix} \\ & \times e^{-j2\pi d_{s_1,s_2} f/c}, \end{aligned} \tag{16}$$

$$\begin{aligned} H_{ij,\mathrm{mobile}}^{s_{\mathrm{m}}} = & \begin{bmatrix} E_{\mathrm{V},i}^{\mathrm{Rx}}(\phi_{\mathrm{AoA}}^{s_{\mathrm{m}}}) \\ E_{\mathrm{H},i}^{\mathrm{Rx}}(\phi_{\mathrm{AoA}}^{s_{\mathrm{m}}}) \end{bmatrix}^{T} \boldsymbol{\alpha}_{\mathrm{mobile}}^{s_{\mathrm{m}}} \begin{bmatrix} E_{\mathrm{V},j}^{\mathrm{Tx}}(\phi_{\mathrm{AoD}}^{s_{\mathrm{m}}}) \\ E_{\mathrm{H},j}^{\mathrm{Tx}}(\phi_{\mathrm{AoD}}^{s_{\mathrm{m}}}) \end{bmatrix} \\ & \times e^{-j2\pi d_{s_{\mathrm{m}1}} f/c}, \end{aligned} \tag{17}$$

where $\boldsymbol{\alpha}_{\mathrm{diffuse}}^{s_{\mathrm{s}}}$, $\boldsymbol{\alpha}_{\mathrm{diffuse}}^{s_1 s_2}$ and $\boldsymbol{\alpha}_{\mathrm{mobile}}^{s_{\mathrm{m}}}$ are the polarimetric path amplitude matrices defined in (8), (11) and (12) respectively. The path distances d_{s1},d_{s_1,s_2} and $d_{s_{\mathrm{m}1}}$ are defined in Section IV-A.

The model parameters, i.e., the density and RCS of the mobile and diffuse scatterers are manually optimised by heuristically comparing with the measured channel characteristics described in Section III. As we consider up to second order diffuse scattering, many multipath components arrive at the same delay bin. Thus, the fading characteristics are an inherent part of the model.

C. Implementation recipe

The implementation of the channel model involves generating the scatterers, followed by calculating the path parameters, i.e., power, amplitude, AoA and AoD. Finally the band-limited channel transfer function matrix $\boldsymbol{H}$ is generated combining the paths. Realistic model parameters based on [29] are considered for the simulations as listed in Table I, with the geometrical settings defined in Fig. 6. The implementation steps are summarized as follows.

1) Simulate using an electromagnetic solver, or measure the mutual coupling $H_{ij,\mathrm{direct}}$ between the Tx and Rx antennas of the IBFD relay.
2) Define the Tx/Rx antenna position and the smooth building walls along the x-coordinate as well as room walls. Assign corresponding permittivities and derive their normal vectors.
3) Generate diffuse and mobile scatterers as shown in the layout in Fig. 6 and assign RCS to them based on the type of scatterers.

TABLE I
LIST OF PARAMETERS FOR THE SI CHANNEL MODEL

Parameter	Value	Parameter	Value
λ_{fast}	$0.4\,\text{m}^{-1}$	W_{road}	19.4 m
λ_{slow}	$0.2\,\text{m}^{-1}$	W_{p1}	5.95 m
λ_{diffuse}	$2\,\text{m}^{-1}$	W_{p2}	2.92 m
σ_{fast}	$100\,\text{m}^2$	W_{L1}	3.67 m
σ_{slow}	$1\,\text{m}^2$	W_{L2}	3.67 m
σ_{diffuse}	$1\,\text{m}^2$	W_{L3}	3.59 m
$v_{\text{max}}^{\text{slow}}$	$1.39\,\text{ms}^{-1}$	W_{room}	8 m
v_{fast}	$5\,\text{ms}^{-1}$	D_{room}	8 m
CPR	0 dB	d_{break}	94.4 m
XPD_{V}	17 dB	XPD_{H}	17 dB

4) Assign velocities to the mobile scatterers depending on the traffic lane, which classifies pedestrians and vehicles.
5) Compute Fresnel reflection coefficients from the smooth walls up to N_{w}-th order reflections.
6) Identify the first and second order scattered paths from the diffuse scatterers along the smooth walls.
7) Derive the first order scattered paths from the mobile scatterers using their current position.
8) Calculate the transfer function of each path from the smooth walls $H^{l}_{ij,\text{wall}}$, diffuse scatterers $H^{s}_{ij,\text{diffuse}}$, $H^{s_1 s_2}_{ij,\text{diffuse}}$, and mobile scatterers $H^{s_{\text{m}}}_{ij,\text{mobile}}$ using (14)-(17) combining the antenna gain with the complex amplitude of each path.
9) Calculate the channel transfer function as described in (13) combining the transfer function of all the paths, depending on the desired system bandwidth and frequency spacing.
10) Update the position of the mobile scatterers for the next timestep.
11) Compute the updated transfer function for the paths due to mobile scatterers, $H^{s_{\text{m}}}_{ij,\text{mobile}}$ and repeat steps 9)-11) for all remaining timesteps.

V. CHANNEL MODEL VALIDATION

In this section, the delay, Doppler and spatial characteristics of the SI channel generated by the proposed model are compared with the measurements. Fifty different realisations of the mobile scatterers are simulated with the co-located Tx/Rx antenna located 30 cm away from the wall. The glass window next to the antenna has a permittivity $\epsilon_r = 6.5$ and the building walls along the road and adjacent room walls are defined as concrete, $\epsilon_r = 4$. As the measurement site was overlooking a side road parking bay, there is no building exactly opposite to the wall, as shown in Fig. 4. Hence, a smooth wall recessed from the building line by $D_{\text{park}} = 4.56$ m, corresponding to the wind shield of a car parked in the parking bay is considered in the simulations. The recessed smooth wall is modelled as glass windows with permittivity $\epsilon_r = 6.5$. The initial positions of the mobile scatterers are then generated in the respective lanes with corresponding velocities. Fig. 7 shows an exemplary geometry for a single time instant, where the diffuse scatterers are located adjacent to the smooth walls. The channel transfer functions (13) are derived for the same frequency band as

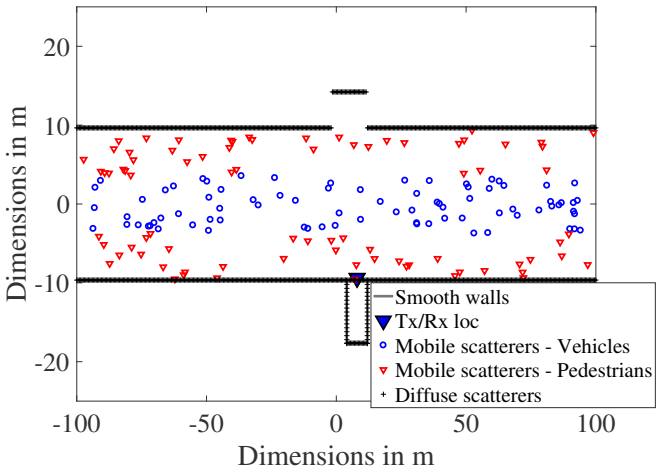

Fig. 7. Sample geometry with scatterer positions. The scale along the x and y dimensions are different to each other.

TABLE II
COMPARISON OF MEAN DELAY AND RMS DELAY SPREAD BETWEEN MEASUREMENTS AND SIMULATIONS

Polarization	Mean delay (ns)		RMS Delay spread (ns)	
	Measured	Simulated	Measured	Simulated
V-V	7.09	8.96	12.7	14.5
H-H	5.82	6.59	8.48	11.1
V-H	6.81	7.18	9.55	8.17
H-V	9.42	4.90	14.5	8.29
Global	6.50	7.53	10.7	12.3

measurements, i.e., between 2.45 and 2.75 GHz with 0.5 MHz resolution. The IFFT of the transfer function results in the band-limited CIRs.

A. Delay domain

Fifty CIRs are generated from each scatterer realization by adding random phases to each path to account for small-scale fading effects. The *polarisation-specific* PDPs are then calculated by incoherently averaging the 50 CIRs over different realisations of the mobile scatterers. Finally, the *global* PDPs are derived as the average of the *polarisation-specific* PDPs. Fig. 8 compares the measured and simulated PDPs according to the polarisations. The PDPs show agreement of their shapes between our simulations and measurements. The specular PDPs in Fig. 8 show that the channel model can reproduce the propagation phenomenon in the measured deployment scenario, reproducing the measured peaks. In addition to the specular peak due to reflection from the recessed wall on the opposite side of the road, the model also includes diffuse scattering from the opposite side of the road. This causes additional SI near the specular peak. The difference between the simulated and measured *global* RMS delay spread is 1.6 ns, which is less than the delay resolution of the measurement, 3.33 ns. Table II compares the simulated and measured mean delay and RMS delay spreads, indicating the validity of the model.

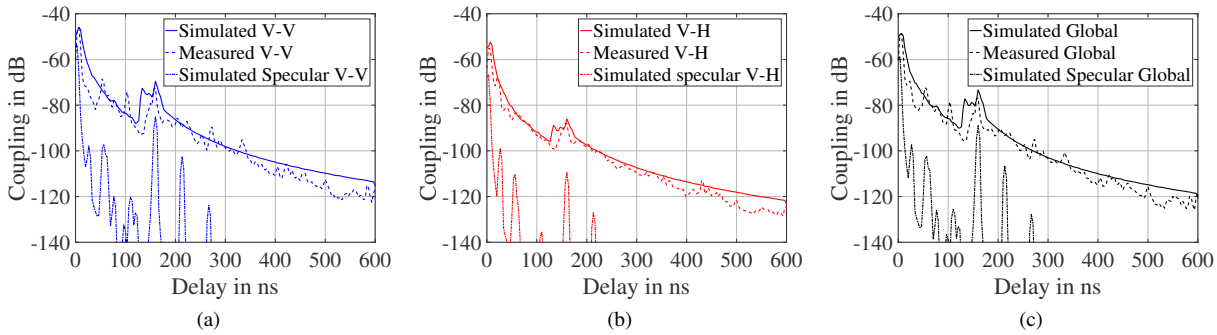

Fig. 8. Comparison of simulated and measured PDPs for (a) V-V (b) V-H polarisations of antennas and (c) *global* PDPs along with those derived from specular reflections only for the respective polarisations. The simulated PDPs for the H-H and H-V polarised combinations also follow the measurements but are not shown due to space constraint.

The fading characteristics are studied in a similar manner as described in Section III-A with the fading realizations from the 50 CIRs of the MIMO channel for different scatterer realisations. The simulated Ricean K-factors are 6.8 dB and 4.8 dB for the first two delay bins at 0 ns and 3.33 ns, compared to 5.1 dB and 0.3 dB from measurements, respectively. The remaining delay bins undergo Rayleigh fading. The small difference in the first two delay bins between the measured and simulated characteristics can be attributed to the near field scattering which is not considered in the model.

B. Doppler domain

For each of the 50 different scatterer realisations, the mobile scatterers are displaced according to their velocity, every 7 ms for 350 ms period. The paths characteristics, i.e., delay, amplitude, AoA and AoD from the mobile scatterers, are updated and the corresponding CIRs are obtained for each time step. We therefore have 50 different time-varying sets of CIRs. They are converted to the spreading functions, whereby RMS Doppler spreads are derived for each delay bin. The averaged RMS Doppler spreads over 50 different realizations of mobile scatterers and over *co-* and *cross-* polarisations of the Tx and Rx antenna feeds are shown in Fig. 9. The figure indicates good agreement between the simulated and measured RMS Doppler spreads. Although we assume fixed installation of the relays as they are infrastructure devices, the simulated and measured average RMS Doppler spreads in Fig. 9 indicate that our proposed channel model reproduces the non-stationarity of the measured channel with the pedestrians and vehicles in the surrounding environment.

C. Spatial domain

Finally, we compare the simulated and measured narrowband antenna correlation on the Tx and Rx sides. The channel transfer functions at the first time step in the Doppler validation, i.e., the initial positions of the mobile scatterers defined in Section V-B, are used. The antenna correlation is calculated in a similar manner as described in Section III-C, where the average of narrowband antenna correlation values is taken over antenna elements on the other side, the radio frequency and

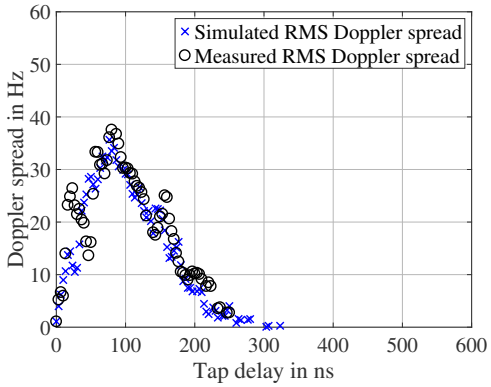

Fig. 9. Simulated and measured *global* RMS Doppler spread for each delay bin.

the 50 realisations of mobile scatterers. The result gives us the same conclusion as measurements that the narrowband antenna correlation is always less than 0.6 and hence insignificant.

VI. Conclusion

Here we have presented new channel measurements for SI coupling between Tx and Rx elements of an IBFD relay antenna system, and developed a site-specific GSCM which can replicate the observed propagation phenomena. The SI channel was characterized in an outdoor street-canyon deployment scenario and a two-dimensional site-specific GSCM is proposed for modelling the wideband dynamic MIMO SI channels. The measured SI channel characteristics between 2.45-2.75 GHz indicate that a significant portion of the SI arrives within 10.7 ns, corresponding to the first four delay bins with 3.33 ns spacing. It was found that objects in the near vicinity of the antenna, such as windows, contribute significantly to the SI. Thus, mitigating the SI in the first four delay bins in the analogue/RF domain can decrease the load on additional baseband cancellation techniques. The measured Doppler characteristics show that maximum Doppler spread is 41 Hz due to vehicular movement in the environment. Finally, the transmit and receive antennas of the on-frequency repeater are uncorrelated. This indicated that eigenmode based

cancellation solutions may not be effective for MIMO with a limited number of antenna elements as the multipath SI arrives from all directions.

The proposed GSCM for the SI channel considers smooth walls producing specular reflections, objects near the smooth walls, along with mobile scatterers which model diffuse scattering from pedestrians and vehicles. The proposed SI channel model is the first channel model based on measurements to simulate the SI channel jointly in the polarization, delay, Doppler and spatial domains, all of which are critical in the development and evaluation of IBFD radios. The model was validated through comparison with measurements at 2.6 GHz.

REFERENCES

[1] S. Chen *et al.*, "Division-free duplex for wireless applications," *Electronics Letters*, vol. 34, no. 2, pp. 147–148, Jan. 1998.

[2] A. Sahai *et al.*, "Pushing the limits of full duplex wireless: design and real-time implementation," Rice Univ. Houston, TX, Tech. Rep. TREE1104, 2011. [Online]. Available: http://arxiv.org/abs/1107.0607

[3] B. P. Day *et al.*, "Full-duplex MIMO relaying: Achievable rates under limited dynamic range," *IEEE J. Sel. Areas Commun.*, vol. 30, no. 8, pp. 1541–1553, Sep. 2012.

[4] D. Bharadia *et al.*, "Full duplex radios," *SIGCOMM Comput. Commun. Rev.*, vol. 43, no. 4, pp. 375–386, Aug. 2013.

[5] D. Korpi *et al.*, "Advanced self-interference cancellation and multi-antenna techniques for full-duplex radios," in *2013 Asilomar Conf. Signals, Syst. Comput.*, Nov. 2013, pp. 3–8.

[6] A. Sabharwal *et al.*, "In-band full-duplex wireless: Challenges and opportunities," *IEEE J. Sel. Areas Commun.*, vol. 32, no. 9, pp. 1637–1652, Sep. 2014.

[7] L. Laughlin *et al.*, "Optimum single antenna full duplex using hybrid junctions," *IEEE J. Sel. Areas Commun.*, vol. 32, no. 9, pp. 1653–1661, Sep. 2014.

[8] E. Everett *et al.*, "Passive self-interference suppression for full-duplex infrastructure nodes," *IEEE Trans. Wireless Commun.*, vol. 13, no. 2, pp. 680–694, Feb. 2014.

[9] S. Hong *et al.*, "Applications of self-interference cancellation in 5G and beyond," *IEEE Commun. Mag.*, vol. 52, no. 2, pp. 114–121, feb 2014.

[10] L. Laughlin *et al.*, "Electrical balance duplexing for small form factor realization of in-band full duplex," *IEEE Commun. Mag.*, vol. 53, no. 5, pp. 102–110, May 2015.

[11] T. Huusari *et al.*, "Wideband self-adaptive RF cancellation circuit for full-duplex radio: Operating principle and measurements," in *2015 IEEE 81st Veh. Tech. Conf. (VTC Spring)*, May 2015, pp. 1–7.

[12] K. Haneda *et al.*, "Design and implementation of full-duplex transceivers," in Ch. 17 of *Signal Processing for 5G*, F.-L. Luo and C. Zhang, Eds. John Wiley & Sons, Ltd, 2016, pp. 402–428.

[13] M. Heino *et al.*, "Recent advances in antenna design and interference cancellation algorithms for in-band full duplex relays," *IEEE Commun. Mag.*, vol. 53, no. 5, pp. 91–101, May 2015.

[14] G. Liu *et al.*, "In-Band Full-Duplex Relaying: A Survey, Research Issues and Challenges," *IEEE Commun. Surv. Tutorials*, vol. 17, no. 2, pp. 500–524, 2015.

[15] M. Alleven, "Deutsche Telekom completes 5G full duplex field trial with Kumu Networks," Fierce Wireless Magazine, Sep. 2015. [Online]. Available: http://www.fiercewireless.com/tech/deutsche-telekom-completes-5g-full-duplex-field-trial-kumu-networks

[16] Y. Sudoh *et al.*, "Prototype system evaluation and field trial of 40 ghz-band directional division duplex (DDD) radio system," in *2016 International Symposium on Antennas and Propagation (ISAP)*, Oct 2016, pp. 592–593.

[17] L. Laughlin *et al.*, "Passive and active electrical balance duplexers," *IEEE Trans. Circuits Syst. II Express Briefs*, vol. 63, no. 1, pp. 94–98, Jan. 2016.

[18] M. Duarte and A. Sabharwal, "Full-duplex wireless communications using off-the-shelf radios: Feasibility and first results," in *Forty Fourth Asilomar Conference on Signals, Systems and Computers (ASILOMAR)*, 2010, pp. 1558–1562.

[19] M. Duarte *et al.*, "Experiment-driven characterization of full-duplex wireless systems," *IEEE Trans. Wireless Commun.*, vol. 11, no. 12, pp. 4296–4307, 2012.

[20] L. Laughlin *et al.*, "Dynamic performance of electrical balance duplexing in a vehicular scenario," *IEEE Antennas Wireless Propag. Lett.*, 2016.

[21] K. Haneda *et al.*, "Measurement of loop-back interference channels for outdoor-to-indoor full-duplex radio relays," in *Proc. Fourth European Conf. on Ant. Prop. (EuCAP 2010)*, 2010, pp. 1–5.

[22] S. N. Venkatasubramanian *et al.*, "Wideband self-interference channel modelling for an on-frequency repeater," in *10th European Conf. on Ant. Prop. (EuCAP 2016)*, Apr. 2016, pp. 1–5.

[23] J. Karedal *et al.*, "A geometry-based stochastic MIMO model for vehicle-to-vehicle communications," *IEEE Trans. Wireless Commun.*, vol. 8, no. 7, pp. 3646–3657, Jul. 2009.

[24] J. Medbo *et al.*, "Radio propagation modeling for 5G mobile and wireless communications," *IEEE Commun. Mag.*, vol. 54, no. 6, pp. 144–151, June 2016.

[25] A. F. Molisch, *Wireless Communications, 2nd Edition*. Wiley-IEEE Press, 2010.

[26] L. Greenstein *et al.*, "Moment-method estimation of the Ricean K-factor," *IEEE Commun. Lett.*, vol. 3, no. 6, pp. 175–176, June 1999.

[27] T. Riihonen *et al.*, "Mitigation of Loopback Self-Interference in Full-Duplex MIMO Relays," *IEEE Trans. Signal Process.*, vol. 59, no. 12, pp. 5983–5993, Dec. 2011.

[28] M. J. Feuerstein *et al.*, "Path loss, delay spread, and outage models as functions of antenna height for microcellular system design," *IEEE Trans. Veh. Technol.*, vol. 43, no. 3, pp. 487–498, Aug. 1994.

[29] M. I. Skolnik, *Introduction to radar systems*, second edition ed. Auckland: McGraw-Hill, 1980.

Sathya N. Venkatasubramanian received the M.Sc. (Tech.) degree in radio science and engineering from Aalto University, Espoo, Finland, in 2013, and D.Sc. (Tech.) degree in Radio Engineering in 2018. His current research interests include antennas, propagation and spectrum aspects in future wireless systems.

Chunqing Zhang received the B.Eng and M.Sc.degree in Telecommunication and Information Systems from Beijing Jiaotong University, Beijing, China, in 2001 and 2004, and the Ph.D degree in Communications Engineering from the University of Bristol, Bristol, U.K., in 2018. Between 2004 to 2014, he was working in the R and D department of Datang Mobile Telecommunication Equipment Ltd, Beijing, China. He is currently working at Huawei Technologies Ltd, Shenzhen, China. His research interests are in wireless communications and IoT.

Leo Laughlin received the M.Eng. degree in Electronic Engineering from the University of York, York, U.K., in 2011, and the Ph.D degree in Communications Engineering from the University of Bristol, Bristol, U.K., in 2016. In 2009-10 he was at Qualcomm in Farnborough, U.K., working on Physical Layer DSP for GSM receivers. In 2011 he was at Omnisense Ltd in Cambridge, working on radio geolocation systems. He is currently a Research Fellow in the Communications Systems and Networks Laboratory at the University of Bristol. His research interests are in tunable and reconfigurable radio technologies for mobile devices.

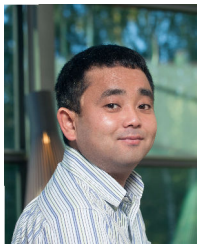

Katsuyuki Haneda (S'03, M'07) received the Doctor of Engineering from the Tokyo Institute of Technology, Tokyo, Japan, in 2007. Dr. Haneda is presently an associate professor in Aalto University School of Electrical Engineering. He is the author and co-author of a number of best paper awards in IEEE Vehicular Technology Conference, European Conference on Antennas and Propagation and Loughborough Antennas and Propagation Conference, including student paper awards. Dr. Haneda has been an associate editor of the IEEE Transactions on Antennas and Propagation between 2012 and 2016, and of an editor of the IEEE Transactions on Wireless Communications since 2013. He has also been an active member of a number of European COST Actions, e.g., CA15104 "Inclusive Radio Communication Networks for 5G and beyond (IRACON)", where he is a co-chair of a disciplinary working group on radio channels. His current research activity includes high-frequency radios such as millimeter-wave and beyond, wireless for medical, post-disaster scenarios and internet-of-things, and in-band full-duplex radio technologies.

Mark Beach received his PhD for research addressing the application of Smart Antenna techniques to GPS from the University of Bristol in 1989, where he subsequently joined as a member of academic staff. He was promoted to Senior Lecturer in 1996, Reader in 1998 and Professor in 2003. He was Head of the Department of Electrical and Electronic Engineering from 2006 to 2010, and then spearheaded Bristol's hosting of the EPSRC Centre for Doctoral Training (CDT) in Communications. He currently manages the delivery of the CDT in Communications, leads research in the field of enabling technologies for the delivery of 5G and beyond wireless connectivity, as well as his role as the School Research Impact Director. Mark's current research activities are delivered through the Communication Systems and Networks Group, forming a key component within Bristol's Smart Internet Lab. He has over 25 years of physical layer wireless research embracing the application of Spread Spectrum technology for cellular systems, adaptive or smart antenna for capacity and range extension in wireless networks, MIMO aided connectivity for through-put enhancement, Millimetre Wave technologies as well as flexible RF technologies for SDR modems underpins his current research portfolio.